







Research report

Biomechanical simulations of intracerebral hemorrhage expansion show tissue displacement has significant impact on electrical impedance tomography results



Antti Paldanius^{a,*}, Jussi Toivanen^{b,2}, Nina Forss^{c,d,3}, Daniel Strbian^{c,4},
Ville Kolehmainen^{b,5}, Jari Hyttinen^{a,6}

^a Faculty of Medicine and Health Technology, Tampere University, Kalevantie 4, Tampere 33720, Finland

^b Department of Technical Physics, University of Eastern Finland, Yliopistonranta 8, Kuopio 70210, Finland

^c HUS Neurocenter, Helsinki University Hospital, Helsinki, Finland

^d Department of Neuroscience and Biomedical Engineering, Aalto University, Rakentajanaukio 2, Espoo 02150, Finland

ARTICLE INFO

Keywords:

Brain imaging
Electrical impedance tomography (EIT)
Hematoma expansion (HE)
Intracerebral hemorrhage (ICH)
Stroke imaging
Stroke monitoring
Biomechanical model of ICH

ABSTRACT

Objective: Intracerebral hemorrhage (ICH) occupies intracranial space and causes brain tissue displacement and fluid volume shifts. We assess how hematoma expansion (HE) affects electrical impedance tomography (EIT) measurements and reconstructed images of the conductivity change caused by HE.

Methods: We developed a novel multi-physics model of ICH with mechanical tissue deformation during HE. We simulated EIT measurements with the multi-physics model and a traditional static model using five ICH locations. The effects of tissue deformation on the results of monitoring of ICH with EIT were assessed by comparing the measurement data from the multi-physics and traditional models and by comparing the corresponding reconstructed conductivity change from two image reconstruction algorithms.

Results: The simulated measurement data and the reconstructed images of the conductivity change using the multi-physics and the traditional model are radically different regardless of the image reconstruction algorithm used.

Conclusions: The effect of tissue displacement caused by HE on EIT monitoring of ICH is significant. Specifically, the displacement of cerebrospinal fluid (CSF) can mask the effects of increased ICH blood volume. However, the effects of displaced CSF could be easier to detect with EIT than the ICH blood volume increase and thus could be used as an indicator of HE in EIT bedside monitoring of ICH and improve the detectability of HE, especially for ICH located deep in the brain.

Significance: Currently there are virtually no imaging methods for continuous monitoring of stroke. There has been recent resurgence in interest to develop electrical impedance tomography (EIT) devices and algorithms for monitoring progression of stroke. In-silico studies show promising results, but there are very little clinical results. In-silico models are usually used for development and evaluation of algorithms for EIT image reconstruction. In previous studies the stroke has been usually modeled as local change in electrical conductivity and the fluid and tissue displacement caused by the increased blood volume in ICH has not been considered. In this paper we present a novel multi-physics model of ICH, simulated EIT measurement results and reconstructed images with comparisons to the traditionally used ICH modeling methods. Our multi-physics approach to modeling of ICH shows that the effect of tissue and fluid displacement during HE needs consideration when developing clinical applications of EIT.

* Corresponding author.

E-mail address: antti.paldanius@tuni.fi (A. Paldanius).

¹ ORCID: 0000-0001-9560-172X.

² ORCID: 0000-0002-3383-4373.

³ ORCID: 0000-0002-1620-8573.

⁴ ORCID: 0000-0001-9095-2344.

⁵ ORCID: 0000-0002-5621-795X.

⁶ ORCID: 0000-0003-1850-3055.

1. Introduction

Stroke is the second leading cause of death worldwide and is a significant cause of disability (Katan and Luft, 2018). Intracerebral hemorrhages (ICH) account for 10–30 % of all acute strokes and are associated with very high morbidity and mortality (Renado et al., 2024; Poon et al., 2014; Pinho et al., 2019). Unlike for ischemic stroke, no single intervention has unequivocally been shown to improve functional outcomes for ICH. The treatment of ICH is based on the best possible medical treatment, and in the most severe cases on neurosurgical intervention (Greenberg et al., 2022). One of the strongest predictors of functional outcome is the initial ICH volume (Broderick et al., 1993) and the subsequent hematoma expansion (Mayer et al., 2021).

Hematoma expansion (HE) occurs in about 70 % of ICH patients and occurs usually during the first couple of hours after the initial event (Davis et al., 2006). Hematoma expansion in ICH patients is currently detected with computed tomography (CT). Such imaging is understandably intermittent, prompted by changes in patient's clinical signs and symptoms, or according to fixed timing of control CTs (Greenberg et al., 2022). The unmet clinical need for real-time detection of HE has prompted a search for suitable bedside imaging modalities. In addition to bedside head CT scanning, which is still relatively rare and has some limitations (Goertz et al., 2024), there has been recent interest in developing electrical impedance tomography (EIT) for bedside HE monitoring (Toivanen et al., 2024; Ouyppornkochagorn et al., 2023; Shi et al., 2021; Yang et al., 2017; Dai et al., 2013; Xu et al., 2010).

In EIT monitoring, HE has been considered to be detectable as electrical conductivity changes that are caused by the increased volume of blood (Toivanen et al., 2024; Ouyppornkochagorn et al., 2023; Shi et al., 2021; Yang et al., 2017; Dai et al., 2013; Xu et al., 2010). In EIT these conductivity changes are reconstructed based on electrical measurements of the patient's head. In the measurement setup, a set of electrodes are attached to the patient's head. Then small and safe alternating currents are fed through a selected set of electrodes and the resulting voltages are recorded on all electrodes. These measurements are then repeated, potentially even within seconds, and the two sets of measurement are used to reconstruct the conductivity changes that have occurred between the measurement sets. EIT is inexpensive, radiation-free and in theory suitable for continuous bedside monitoring of ICH, although that has yet to be shown in a clinical setting.

Simulation based EIT studies use computational head models to simulate the EIT measurements. Such models have traditionally been three-layer or otherwise simplified models (Li et al., 2017; Ouyppornkochagorn et al., 2023) or more realistic six-or-more-layer models (Paldanius et al., 2021; Jehl et al., 2016). However, these models use

tissue swapping within fixed tissue boundaries to simulate HE, and are thus ignoring key phenomenon of HE: the mass effect and sulcal effacement.

Mass effect is the phenomenon in which a lesion or contusion, in this case ICH and HE, takes up space within the restricted skull space and causes the surrounding brain tissues to be compressed and even injured. Sulcal effacement is a consequence of mass effect; compression of brain tissues pushes adjacent gyri together and cerebrospinal fluid (CSF) gets pushed out of the sulci (Fig. 1). Following the Monro-Kellie's hypothesis (Mokri, 2001) that states that the sum of volumes of brain, CSF and intracranial blood is constant, sulcal effacement results in reduction in total CSF volume within the cranium (Mokri, 2001), given that CSF and blood are the only components capable of leaving the cranium. A simulation model of mass effect has been previously described in literature in simulation of ischemic stroke development (Bing et al., 2020) and deformation of brain tissues has been simulated in relation to tumor growth (Angeli and Stylianopoulos, 2016).

Reduction of CSF volume is extremely relevant to EIT monitoring of HE. The conductivity of CSF is around 2.0 S/m and the conductivity of blood is around 0.7 S/m (Gabriel et al., 1996). Therefore, reduction in CSF volume might overpower perceived conductivity changes from changes in blood volumes caused by HE, especially with ICH deep within the brain tissues. This initially unintuitive conductivity decrease caused by hemorrhagic strokes have been noted in some stroke EIT literature, see e.g. Goren, 2020; Dai et al., 2018; Yang et al., 2017, and have been speculated to result from displacement of CSF. Our previous simulation study (Paldanius et al., 2021) has shown that CSF is critically important for accurately simulating EIT measurements.

In this paper, our aim is to assess how the tissue displacement and geometrical changes during HE affect the EIT measurement and the subsequent EIT image reconstruction of the conductivity change resulting from HE between two measurements. For this we introduce a novel multi-physics in-silico head model for EIT measurement data simulation. This model combines simulation of the mass effect, sulcal effacement and CSF volume reduction caused by HE with electrical simulation of the EIT measurement. We compare the results from our multi-physics model to results from the traditional, undeformable, tissue-swapping based head model introduced in (Paldanius et al., 2021). We test two EIT image reconstruction algorithms to see how these geometric effects are observed in EIT reconstructions of the conductivity change to assess detectability of the changes caused by HE in EIT based monitoring of ICH.

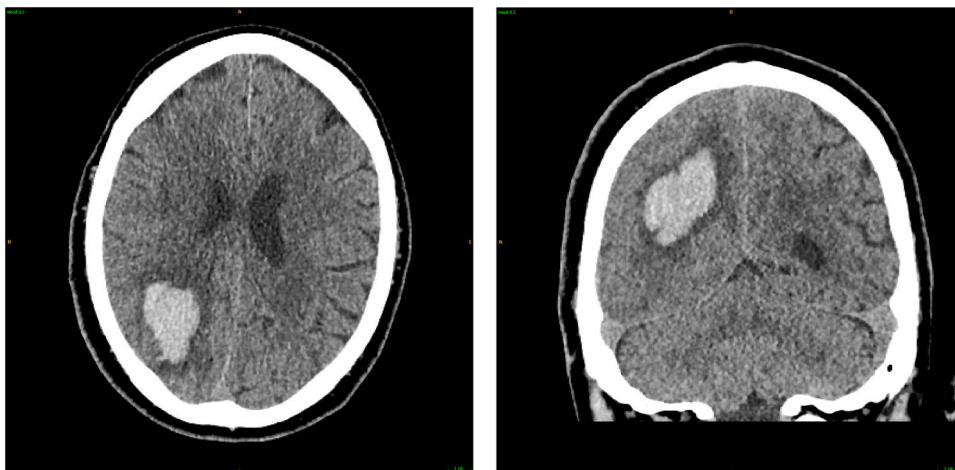


Fig. 1. Sulcal effacement in an ICH patient. Right hemisphere of the brain has normal anatomy, the left exhibits sulcal effacement caused by an ICH lesion and associated swelling. The volume of the ICH lesion was measured to be 18 ml.

2. Materials and methods

2.1. Head model

In this study, two different modeling approaches were used in EIT data simulation to study the effect of tissue displacement on EIT measurements and reconstructions. For purposes of this study, we developed a multi-physics model, which uses the novel approach of simulating the biomechanics of tissues and their deformation caused by hematoma expansion (Fig. 2). The reference model uses the traditional approach of simply using static geometry and inserting a lesion of blood in the brain parenchyma. For comparability, the same finite element meshes were used with both models. In the traditional model the size of the ICH lesion was increased by swapping the material in a small volume surrounding the original lesion from white matter to blood. In the multi-physics model, the deformation of the tissues caused by HE is simulated. The ICH lesion sizes simulated in this study were relatively small, with the initial lesion being 8 ml in volume and growing to 14 ml, which is the median size of ICH lesion reported in literature (Robinson et al., 2022).

2.1.1. Finite element mesh

The segmented geometry used as a basis for the head model was obtained from Population Head Model repository (Lee et al., 2016). These segmentations had anatomically detailed six-layer head models consisting of scalp, skull, CSF, grey matter, white matter and cerebellum. The segmented geometry files were imported into ScanIP Simpleware and any problems with the geometries were manually cleaned up. The original segmented models were missing the dura mater, so an approximation of falx cerebri was created by defining a boundary in the CSF volume between the hemispheres of the brain. Also, 32 circular electrodes with a diameter of 10 mm were defined on the scalp according to the modified 10-5 system for EIT from Goren et al. (2018a). The initial ICH was modeled as a sphere with a 25 mm diameter inside the brain parenchyma. Another sphere with diameter of 30 mm was defined surrounding the 25 mm sphere to enable material swapping when using the traditional model. Based on this geometry, five finite element (FE) meshes of approximately 5 million elements were generated, each with a different location for the ICH. A finer refinement was used around the electrodes and the thin structures, such as the skull. The five finite element meshes were exported to COMSOL Multiphysics 6.1 for the traditional and multi-physics model simulations. Image reconstruction models described later are based on independent conventional

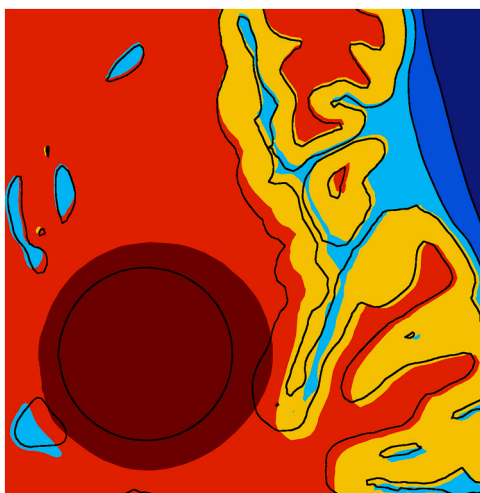


Fig. 2. Example of simulated mechanical deformation of tissues caused by hematoma expansion. 2D slice from 3D model with dark lines denoting the original tissue outlines. Hematoma expansion from 8 ml to 22 ml was used here for illustrative purposes.

discretizations that do not utilize any information of the possible deformations due to the ICH expansion.

2.1.2. Mechanical model

The mechanical model of hematoma expansion used in this study built in the Solid Mechanics interface of COMSOL. As the skull is very rigid compared to the tissues within the cranial cavity, both the skull and the skin were modeled as rigid bodies to save computational resources. Brain tissues were modeled as nearly incompressible hyper-elastic materials using the two parameter Mooney-Rivlin model (Bergström, 2015), where strain energy density is defined by equation;

$$W_s = C_{10}(\bar{I}_1 - 3) + C_{01}(\bar{I}_2 - 3) + \frac{1}{2}\kappa(J_{el} - 1)^2 \quad (1)$$

where C_{10} and C_{01} are the Mooney-Rivlin parameters, κ is the bulk modulus, which for nearly incompressible material was left at the default value of 100 times the initial shear modulus, \bar{I}_1 and \bar{I}_2 are isochoric invariants of the elastic right Cauchy-Green deformation tensors and J_{el} is the elastic volume ratio. The parameters used for different tissues are shown in Table 1.

A thin layer boundary condition was set on the boundary that approximates the location of falx cerebri. The layer was given a thickness of 1 mm and modeled as linear elastic material (Table 2) for which Hooke's law relates the stress tensor to the elastic strain tensor;

$$\sigma = \sigma_{ex} + C : \varepsilon_{el} \quad (2)$$

where C is the 4th order elasticity tensor containing the material properties, “:” is the double-dot tensor product and ε_{el} is the elastic strain and elastic strain energy density is

$$W_s = \frac{1}{2}\varepsilon_{el} : (C : \varepsilon_{el} + 2\sigma_0) \quad (3)$$

where σ_0 is the initial stress.

As a fully-fledged fluid-structure interaction simulation was deemed to be computationally infeasible, the same approach used by Bing et al. (2020) to model the CSF was used in this study to simulate volume change of CSF and blood. Both of these fluids were modeled as compressible hyper-elastic tissues using the parameter shown in Table 1 and bulk modulus $\kappa = 1$ to enable change in the tissue volume. This enabled computationally lighter modeling of the mass effect, sulcal effacement and the CSF volume reduction during an ICH.

The growth of the ICH was modeled by adding a boundary load condition on the boundary between the original lesion and brain tissue;

$$F_A = -pn \quad (4)$$

where F_A is the boundary load vector, p is the pressure and n is the normal of the element. The pressure on the boundary was then gradually increased until the original lesion with diameter of 25 mm and volume of 8 ml would grow to volume of 14 ml and diameter of roughly 30 mm to match the size of the lesion in the traditional model.

Tissue displacement magnitude caused by the hematoma expansion with each of the simulated ICH lesion locations was visualized as semi-transparent 3D volumes and the resulting CSF volume reductions in both hemispheres were measured.

2.1.3. Electrical model

The simulation of EIT measurements was performed using the Electric currents interface in COMSOL in similar fashion as in our previous

Table 1
Linear elastic material properties for falx cerebri (Bing et al., 2020).

Tissue	Density (kg/m ³)	Poisson's ratio	Young's Modulus (MPa)
Falx Cerebri	1133	0.45	31.5

Table 2
Mooney-Rivlin parameters for the tissues (Bing et al., 2020).

Tissue	Density (kg/m ³)	C10 (Pa)	C01 (Pa)
Grey matter	1040	10	500
White matter	1040	45	2200
Cerebellum	1040	10	500
CSF and blood	1000	0.01	50

works (Paldanius et al., 2021; Toivanen et al., 2024). The electrodes were numbered from 1 to 32 (Fig. 3) and 32 independent current injection patterns were setup using MATLAB LiveLink for COMSOL. The contact impedance z_e was set at 2 kΩ for all electrodes. The injection current was set at 1 mA at 1 kHz frequency to match the minimum frequency of the stroke EIT prototype measurement device (Toivanen et al., 2021). The electrical properties for the tissues shown in Table 3 were obtained from literature published by Gabriel et al. (1996).

As the simulations were performed as frequency dependent, COMSOL solves for following equations;

$$\nabla \cdot J = Q_{j,v} \tag{5}$$

where J is the current density and $Q_{j,v}$ is an external current source,

$$J = \sigma E + j\omega D + J_e \tag{6}$$

where σ is the conductivity of the material, E is the electric field, D is the electric displacement field, J_e is external current density,

$$E = -\nabla V \tag{7}$$

and where V is the electric potential.

The electrodes were modeled with a single Neumann boundary condition following the implementation by Fouchard et al. (2015);

$$-n \cdot j = \frac{1}{z_e \|A_e\|} \left(\int_{A_e} V d\Gamma + z_e i_e - \|A_e\| V \right) \tag{8}$$

where $n \cdot j$ is the normal current density, z_e is the contact impedance, i_e is the injected current, A_e is the surface area of the electrode, and V is the electric potential.

Three EIT measurement simulations were performed for each of the

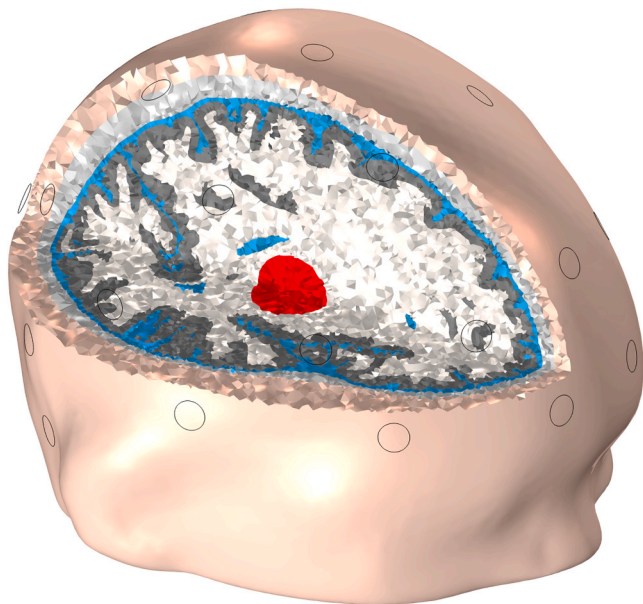


Fig. 3. Electrode locations based on modified 10–5 system (Oostenveld and Praamstra, 2001) for EIT as suggested by Goren et al. (2018b). The cross-section image shows the initial ICH lesion of one of the simulated ICH locations.

Table 3
Dielectric properties of the tissues used in the simulation at 1 kHz frequency (Gabriel et al., 1996).

Tissue	Conductivity (S/m)	Permittivity (F/m)
Scalp	0.32	434,932
Skull	0.02	2702
CSF	2.00	109
White matter	0.06	69,810
Gray matter	0.10	164,062
Cerebellum	0.12	164,358
Blood	0.70	5259

five ICH lesion locations; the initial ICH, hematoma expansion with the traditional approach and hematoma expansion with the multi-physics model. The electrode potentials were extracted in post processing and exported as a.csv table to be used for image reconstruction.

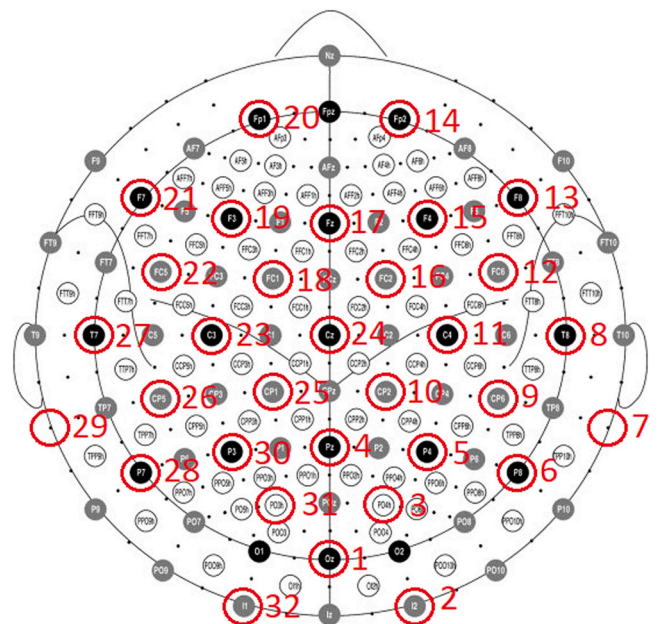
2.2. Reconstruction of conductivity changes

The simulated measurement data from the head models, with added noise, was used to reconstruct 3D images of conductivity changes using the stroke monitoring algorithm from Toivanen et al. (2024) and with the linear difference imaging algorithm from Toivanen et al. (2021, 2024). The noisy realizations of data were obtained by adding Gaussian zero mean random noise with a standard deviation of 0.0184 mV to the simulated noise-free measurements to match the approximated noise level of a prototype stroke EIT measurement device (Toivanen et al., 2024, 2021). For the image reconstructions, the shape of the head and the electrode locations were assumed known and the approximate location of the skull was assumed to be available from a CT image but other structures inside the head were assumed unknown.

For the image reconstruction algorithms, electrode voltages were computed in a mesh of 116,235 nodes and 597,631 elements with refinement near the electrodes as is required for accurate numerical solving. The conductivity was approximated in a coarser mesh of 38,433 nodes and 207,453 elements to give a uniform resolution representation for the unknown image.

2.2.1. Modeling of EIT for image reconstruction

The patient’s head in the EIT measurement setup is modeled as



domain $\Omega \subset \mathbb{R}^3$, and the L electrodes attached to its surface with circular surface patches e_ℓ , $\ell = 1, 2, \dots, L$. The P current injections through selected electrodes are denoted with $I^{(k)} \in \mathbb{R}^L$, $k = 1, 2, \dots, P$, and the corresponding induced voltages on all electrodes are denoted with $U^{(k)} \in \mathbb{R}^L$. Correspondingly, a single current injection is denoted with $I_\ell^{(k)}$ and the corresponding voltages on electrodes with $U_\ell^{(k)}$ for the k th current injection on the ℓ th electrode for $\ell = 1, 2, \dots, L$. With this notation, the conservation of charge and our choice of electric potential ground, we can write

$$\sum_{\ell=1}^L I_\ell^{(k)} = 0 \quad \sum_{\ell=1}^L U_\ell^{(k)} = 0. \quad (9)$$

here, the voltages $U_\ell^{(k)}$ are boundary measurements of the interior electromagnetic potential $u^{(k)}(x)$ that is modeled with the conductivity equation

$$\nabla \cdot (\sigma(x) \nabla u^{(k)}(x)) = 0, \quad x \in \Omega \quad (10)$$

and the boundary conditions of the complete electrode model (Cheng et al., 1989; Somersalo et al., 1992) (CEM) for $k = 1, \dots, P$ and $\ell = 1, \dots, L$

$$u^{(k)}(x) + z_\ell \sigma(x) \frac{\partial u^{(k)}(x)}{\partial n} = U_\ell^{(k)}, \quad x \in e_\ell \quad (11)$$

$$\int_{e_\ell} \sigma(x) \frac{\partial u^{(k)}(x)}{\partial n} dS = I_\ell^{(k)}, \quad (12)$$

$$\sigma(x) \frac{\partial u^{(k)}(x)}{\partial n} = 0, \quad x \in \partial\Omega \setminus \bigcup_{\ell=1}^L e_\ell, \quad (13)$$

where z_ℓ is the contact impedance between the electrode e_ℓ and the body Ω , n denotes the outward unit normal vector on the boundary $\partial\Omega$ and the isotropic conductivity distribution σ is assumed to belong to $L_+^\infty(\Omega) := \{\zeta \in L^\infty(\Omega) \mid \text{ess\,inf} \zeta > 0\}$. The existence and uniqueness of the solution $(u, U) \in H^1(\Omega) \oplus \mathbb{R}^L / \mathbb{R}$ of the model (9)–(13) was proven and its variational form derived in Somersalo et al. (1992).

The aim of the EIT monitoring is to detect the growth of a hemorrhagic stroke as a change in conductivity

$$\delta\sigma = \sigma_2 - \sigma_1 \quad (14)$$

between measurement times t_1 and t_2 . Because the hemorrhage is unlikely to change meaningfully during a single measurement set, the measurements at t_1 and t_2 can both be modeled separately with the stationary model

$$V_i = U(\sigma_i) + e_i, \quad i = 1, 2, \quad (15)$$

where $U(\sigma)$ maps the given conductivity to voltages on the electrodes according to Eqs. (9)–(13), and e models the measurement noise. In this paper, the forward model $U(\sigma)$ is based on the finite element method and details of the implementation can be found in Vauhkonen et al. (1998), Kaipio et al. (2000).

2.2.2. Stroke monitoring algorithm

The stroke monitoring algorithm used in this paper is the same as in Toivanen et al. (2024) and it utilizes non-linear region-of-interest difference imaging (Liu et al., 2015), parallel level sets regularization (Kolehmainen et al., 2019) and a priorconditioned least squares algorithm (Arridge et al., 2014; Harhanen et al., 2015). The algorithm utilizes information from the patient CT that is taken for diagnosis of the stroke at the time of patient admission to the hospital.

The algorithm utilizes a region of interest (ROI) constraint for the conductivity change, so that

$$\text{supp}(\delta\sigma) = \Omega_{\text{ROI}} \subseteq \Omega. \quad (16)$$

The ROI can be chosen based on the patient CT image and for intracerebral hemorrhage monitoring a safe choice that is used also in this paper is to use the full brain volume. Based on the ROI, the conductivity at the later measurement time t_2 is modeled as

$$\sigma_2 = \sigma_1 + K\delta\sigma, \quad (17)$$

where K is an extension mapping that zero-extends the conductivity change from the ROI to the whole domain.

The change in conductivity $\delta\sigma$ between the two measurements V_1 and V_2 is obtained by solving the generalized Tikhonov problem

$$\tilde{\sigma} = \underset{\tilde{\sigma}}{\text{argmin}} \{ \|\tilde{L}_e(\tilde{V} - \tilde{U}(\tilde{\sigma}))\|^2 + p(\tilde{\sigma}) \}, \quad (18)$$

where the diagonal blocks of \tilde{L}_e contain the Cholesky factors of the noise precision matrices of measurements V_1 and V_2 ,

$$\tilde{V} = \begin{bmatrix} V_1 \\ V_2 \end{bmatrix}, \quad \tilde{U} = \begin{bmatrix} U(\sigma_1) \\ U(\sigma_1 + K\delta\sigma) \end{bmatrix}, \quad (19)$$

$$\tilde{\sigma} = \begin{bmatrix} \sigma_1 \\ \delta\sigma \end{bmatrix}, \quad \tilde{e} = \begin{bmatrix} e_1 \\ e_2 \end{bmatrix}, \quad (20)$$

and the regularization functional

$$p(\tilde{\sigma}) = p_{\delta\sigma}(\delta\sigma) + p_{\sigma_1}(\sigma_1) \quad (21)$$

allows independent regularization models for $\delta\sigma$ and σ_1 . We use the same regularization models in this paper as were previously used in studies of stroke monitoring (Toivanen et al., 2021, 2024) that utilize measurement data from static, non-deformable models.

The conductivity change caused by the hemorrhage expanding, and thus our primary unknown $\delta\sigma$, is expected to be localized and regular. Therefore, the regularization model for $\delta\sigma$ is chosen to be the smoothed total variation regularizer (Rudin et al., 1992)

$$p_{\delta\sigma}(\delta\sigma) = TV(\delta\sigma) = \alpha_{\delta\sigma} \int_{\Omega} (\|\nabla\delta\sigma\|^2 + \beta^2)^{1/2} dx, \quad (22)$$

where $\alpha_{\delta\sigma} > 0$ is the regularization weight coefficient, $\nabla\delta\sigma$ is the gradient of the conductivity change and $\beta > 0$ is a small smoothing parameter that ensures differentiability. The values $\alpha_{\delta\sigma} = 5 \cdot 10^{-3}$ and $\beta = 10^{-3}$ were used in this paper.

The secondary unknown σ_1 , the absolute conductivity at measurement time t_1 , is expected to correlate well with the structure of the patient CT. This information is utilized via a parallel level sets based, spatially and directionally weighted smoothed TV regularization that promotes similar alignment of level sets in σ_1 and the CT-based reference image (Kolehmainen et al., 2019), giving

$$p_{\sigma_1}(\sigma_1) = WTV(\sigma_1) = \alpha_{\sigma_1} \int_{\Omega} (\|\nabla\sigma_1\|_{B(\kappa)}^2 + \beta^2)^{1/2} dx, \quad (23)$$

where $\alpha_{\sigma_1} > 0$ is the regularization weight coefficient and the tensor $B(\kappa)$ is chosen such that aligned edges (or level sets) in σ_1 and the reference image κ are preferred. In this paper, the reference image contains only the approximate location of the skull and no other structural information. For more details on the implementation, see Kolehmainen et al., 2019; Toivanen et al., 2021, 2024. The values $\alpha_{\sigma_1} = 10^{-7}$ and $\beta = 10^{-3}$ were used in this paper.

In this paper, the non-linear optimization problem (18) was solved using a lagged Gauss-Newton iteration (Vogel, 2002) equipped with a bounded line search algorithm that enforces $\sigma_1 > 0$ and $\sigma_2 > 0$. The Gauss-Newton search direction was solved using a priorconditioned least squares algorithm (Arridge et al., 2014; Harhanen et al., 2015).

2.2.3. Linear difference imaging algorithm

The linear difference imaging, see e.g. Barber and Seagar, 1987 and Bagshaw et al., 2003, algorithm in this paper aims to reconstruct the change in conductivity $\delta\sigma$ between the two measurements V_1 and V_2 by solving the generalized Tikhonov problem

$$\widehat{\delta\sigma} = \underset{\delta\sigma}{\operatorname{argmin}} \{ \| L_{\delta e}(\delta V - J\delta\sigma) \|^2 + R\delta\sigma \} \quad (24)$$

where $\delta V = V_2 - V_1$, $\delta e = e_2 - e_1$, $L_{\delta e}$ is the Cholesky factor of the noise precision matrix of δe so that $L_{\delta e}^T L_{\delta e} = \Gamma_{\delta e}^{-1} = (\Gamma_{e_1} + \Gamma_{e_2})^{-1}$, the Jacobian matrix J is evaluated at the linearization point σ_0 and R is a linear regularization matrix.

In this paper, as in Toivanen et al. (2021, 2024), the linearization point σ_0 was obtained by solving a non-linear least squares fitting problem for the best fitting spatially constant conductivity using the measurement data V_1 and the linear regularization matrix R was constructed utilizing a distance based correlation model (Lieberman et al., 2010) to create a smoothness promoting regularizer which is a popular choice for linear difference imaging.

3. Results

3.1. Tissue displacement caused by the ICH

Tissue displacement caused by the simulated hematoma expansion from 8 ml to 14 ml volume is visualized in Fig. 4. The tissue displacement is mostly contained within the same hemisphere as the initial ICH. CSF volume reductions caused by the hematoma expansion from 8 ml to 14 ml are presented in Table 4 and likewise, most volume reduction is within the hemisphere with the ICH.

3.2. Measured voltages

Electrode voltage differences $\delta V = V_2 - V_1$ between the approximately 14 ml hemorrhage and the approximately 8 ml hemorrhage computed using the traditional head model and the mechanical head model for the five different hemorrhage locations are shown in Fig. 5. The voltage differences from the traditional head model (top row) are consistently smaller than the corresponding voltage differences from the mechanical head model. In the traditional head model, the voltage difference is caused only by the blood volume replacing brain tissues. In the mechanical model, the voltage difference is dominated by the conductivity change from the displaced CSF and reduced CSF volume.

Table 4

Comparison of simulated CSF volume reduction in the hemisphere with an ICH lesion with hematoma expansion from 8 ml to 14 ml and the hemisphere without a lesion. Units are in milliliters.

ICH location	Right (lesion)	Left (no lesion)
Top	- 3.59	- 2.33
Back	- 3.92	- 2.09
Side	- 3.87	- 2.1
Front	- 3.68	- 2.34
Deep	- 4.48	- 1.8

3.3. Reconstructed conductivity changes

Conductivity changes $\delta\sigma$ reconstructed using the stroke monitoring algorithm are shown in Fig. 6 as semi-transparent 3D volumes. All traditional model reconstructions (top row) show a relatively well defined and limited positive change caused by the increase in blood volume. In contrast, the multi-physics model reconstructions (bottom row) show a wider, closer to the surface negative change caused by the decrease in CSF volume. With the multi-physics model, the negative change in conductivity is completely overwhelming the positive change. This is partially because the negative change is larger in magnitude and in volume, and partially because it is at least partially happening closer to the electrodes than the positive change, thus having a much larger effect on the electrode voltages.

To show that the reconstruction results are not a quirk of the chosen image reconstruction algorithm, the conductivity changes $\delta\sigma$ reconstructed using the well established linear difference imaging algorithm are shown in Fig. 7 as semi-transparent 3D volumes. These reconstructions, even though they have lower contrast and more background variability than the monitoring algorithm reconstructions, support the earlier findings; there is a clear positive trend in the traditional model reconstructions (top row) from the increase in blood volume and a clear negative trend in the multi-physics model reconstructions (bottom row) from the displaced and reduced CSF.

Reconstructions with different measurement noise levels are shown in the supplementary material to demonstrate that the measurement noise level does not change the fundamental difference seen in the reconstructions when using data from the two different data simulation models.

4. Discussion

Hematoma expansion and surrounding oedema is usually limited to

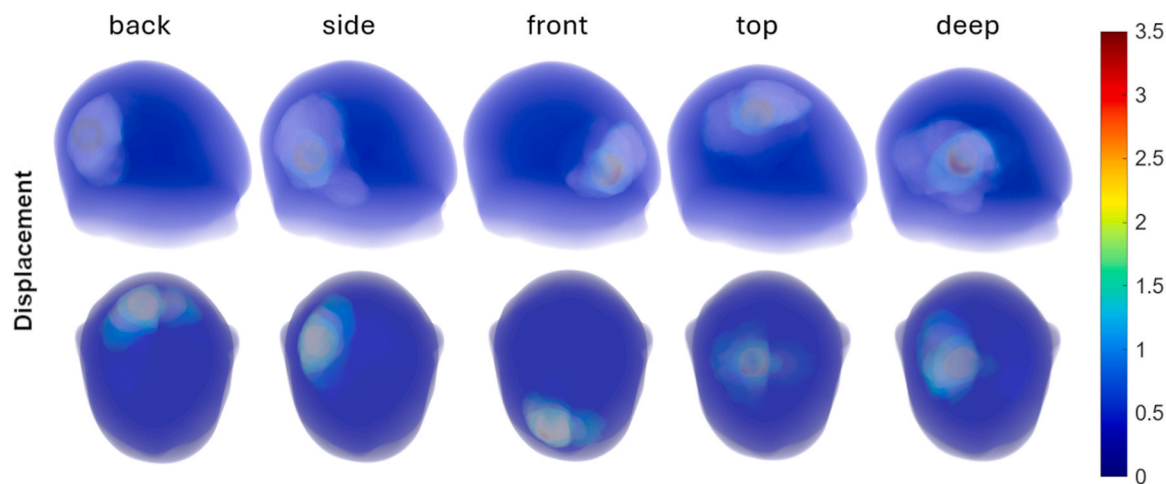


Fig. 4. Tissue displacement induced by hematoma expansion from 8 ml to 14 ml is visualized as semi-transparent 3D volumes. The displacement magnitude is in millimeters. The displacement is strongest near the ICH location but affects a much larger volume than the actual hematoma volume. It is mostly contained within the same hemisphere as the ICH lesion.

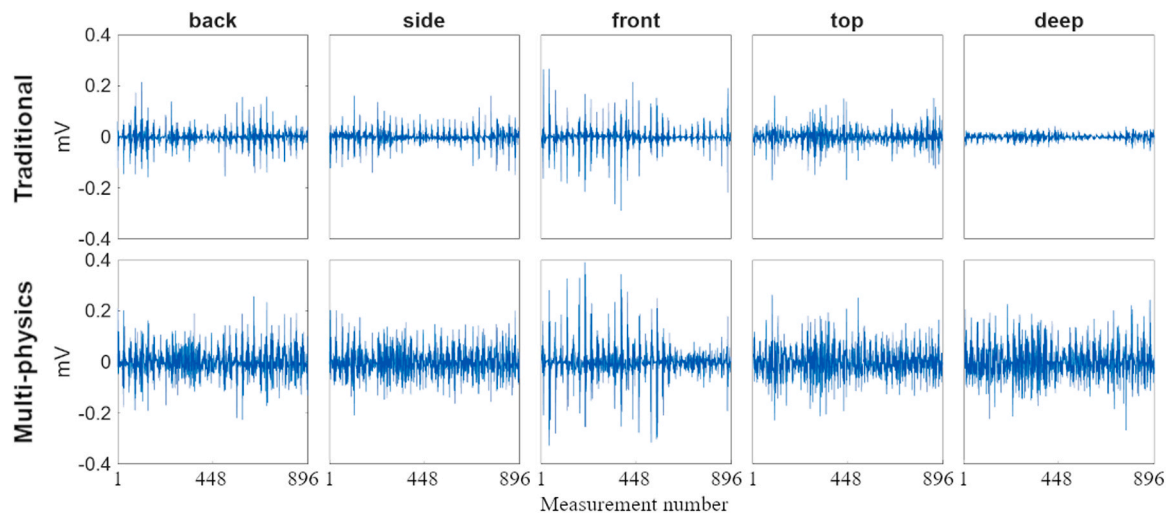


Fig. 5. The effect of hematoma expansion on noise-free simulated measurements visualized using electrode potential difference data $\delta V = V_2 - V_1$ from the traditional head model (top row) and the multi-physics head model (bottom row) for the five different hemorrhage locations. As defined by Eq. (15), V_2 are the simulated electrode potentials after hematoma expansion and V_1 are the simulated electrode potentials during the initial ICH. Each plot contains all simulated electrode potentials on the x-axis, while the y-axis represents how the potentials have changed after the hematoma expansion. Note how δV corresponding to the multi-physics model consistently has larger magnitude compared to δV corresponding to the traditional model, implying that detection of hematoma expansion could be easier from the multi-physics model voltages.

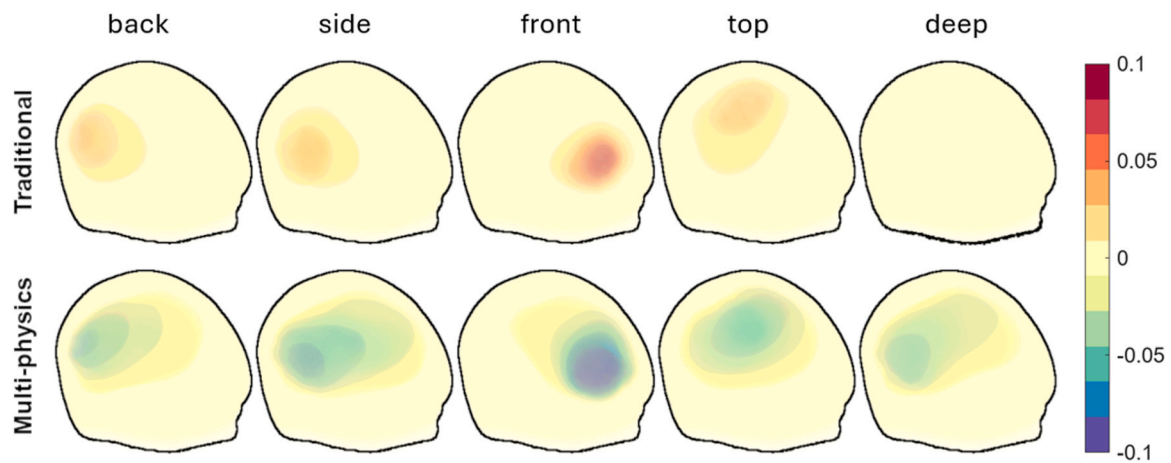


Fig. 6. Conductivity changes reconstructed with the stroke monitoring algorithm using data from the traditional model (top row) and the multi-physics model (bottom row) for the five different hemorrhage locations during hematoma expansion from 8 ml to 14 ml. The reconstructions are visualized as semi-transparent 3D volumes. The traditional model reconstructions show the expansion of the simulated hemorrhage as positive values and the multi-physics model reconstructions show the displaced CSF as negative values that completely overwhelm the positive change from the blood volume increase.

the affected hemisphere. Deformation of brain tissue of the unaffected hemisphere may occur if hemorrhage and oedema of the affected hemisphere occupies space enough to cause a midline-shift. Similar behavior was seen with the CT images (for example Fig. 1) used as reference for this study. The tissue displacement (Fig. 4) caused by the hematoma expansion in our multi-physics model was mostly contained on the same hemisphere as the ICH lesion, giving a good approximation of real-world behavior.

Voltage differences caused by changes in the hemorrhage were clearly larger in the multi-physics model compared to the traditional model (Fig. 5). This implies that the sulcal effacement, even though masking the actual conductivity increase from the increase in blood volume, could make hematoma expansion easier to detect with EIT. This is most evident with the ICH lesion located deep in the brain parenchyma, where in the traditional model the voltage changes are very small. When the tissue displacement simulation is combined with the EIT simulation, the voltage change magnitude produced by hematoma

expansion are similar regardless of lesion location. This was supported by the reconstructions of conductivity change in Figs. 6 and 7 that showed larger changes when using data from the multi-physics model than when using data from the traditional model. This was best shown with the “deep” inclusion location where the change was clearly detectable only when using data from the multi-physics model. The reconstructed images using the monitoring algorithm (Fig. 6) closely resemble the actual tissue displacement in the multi-physics model (Fig. 4), indicating the tissue displacement, especially that of the CSF volume (Table 4), has larger effect on the EIT measurement than the increased conductivity caused by the hematoma expansion.

In previous bio-impedance simulation studies, for example (Ouypornkochagorn et al., 2023; Culpepper et al., 2023; Xiang et al., 2020; Atefi et al., 2016; He et al., 2020), it has been generally assumed ICH or HE would only cause a positive conductivity change. However, conductivity decreases caused by hemorrhagic strokes have been noted in some stroke EIT literature (Goren, 2020; Dai et al., 2018; Yang et al.,

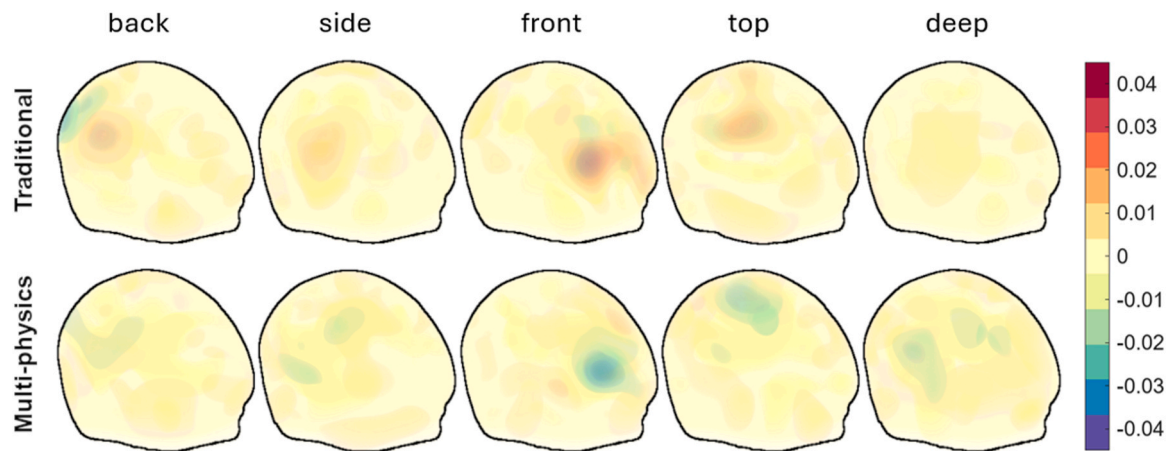


Fig. 7. Conductivity changes reconstructed with the linear difference imaging algorithm using data from the traditional model (top row) and the multi-physics model (bottom row) for the five different hemorrhage locations during hematoma expansion from 8 ml to 14 ml. The reconstructions are visualized as semi-transparent 3D volumes. Note that in addition to the background variability, there is a clear positive trend in the traditional model reconstructions and a clear negative trend in the multi-physics model reconstructions. This shows how the blood volume increase is detected in the traditional model reconstructions and the CSF displacement is detected in the multi-physics model reconstructions.

2017), and have been speculated to result from brain tissues displacing CSF volumes. Simulations performed on our novel multi-physics model and results presented in this article support these earlier speculations on the role of the CSF in EIT measurement of hemorrhagic strokes.

The findings of this study should be considered also when constructing physical phantoms. Even with a realistic head shape and cranial cavity (Avery et al., 2017; Zhang et al., 2017; McDermott et al., 2017), the phantom might give unrealistic result if only a simple conductive element is used to model the ICH and the effects of CSF displacement and volume reduction are ignored.

As computational resources continue to improve, more complex multi-physics approaches to modeling stroke become possible. Our results call for including the effects of tissue deformation into EIT stroke simulations. Future research should include building a fluid-structure interaction type of simulation, which would incorporate reduction of venous blood volume and secondary effects of ICH such as swelling and tissue death near the lesion. Similar modeling approach could be used in evaluating development of ischemic strokes and in studies exploring the capability of EIT in differentiation of ischemic and hemorrhagic strokes.

5. Conclusion

We present a novel multi-physics approach to modeling of electrical impedance tomography (EIT) measurements during intracerebral hemorrhage (ICH) that integrates mechanical tissue deformations caused by hematoma expansion (HE). We studied the effect of tissue displacement caused by HE on reconstructed conductivity change images in EIT. We used simulated EIT measurement data from two different computational head models: a traditional static model with tissue swapping and fixed tissue boundaries, and a multi-physics model that simulates tissue deformation and CSF displacement during ICH expansion. The data from these models was used to reconstruct images of conductivity changes caused by ICH HE and the reconstructions were consistently radically different. The data from the traditional model resulted in relatively well defined and limited positive changes whereas the data from the multi-physics model resulted in a more diffuse negative change.

Comparison of the results from the different models revealed that the effect of CSF displacement caused by HE on reconstructed images is significant and can completely mask the positive conductivity change caused by increased blood volume. The simulated EIT measurement data changed more during HE when tissue displacement was also simulated, implying that the HE could be easier to detect because of the CSF displacement. This is evident especially when the ICH is located deep in

brain parenchyma, such as in basal ganglia.

Our novel multi-physics approach to simulating HE during acute ICH presents a method to improve stroke modeling for development of EIT algorithms. Our work calls for using more accurate data simulation models for simulation-based EIT studies and demonstrates how important it is to consider effects of CSF volume and distribution changes on reconstructed EIT images. Ignoring these effects could even lead to discarding of valid results that do not match the expected result of positive conductivity change during ICH and HE.

Ethical statement

No animal or human subjects were used by authors for the preparation of this manuscript.

Funding sources

This work was supported in part by the Research Council of Finland (Project no. 336791 and no. 353084, Finnish Centre of Excellence in Inverse Modeling and Imaging, Project no. 358944 and no. 359185, Flagship of Advanced Mathematics for Sensing Imaging and Modelling and Project no. 359433 Research Council of Finland proof-of-concept grant, the Jane and Aatos Erkko Foundation and Neurocenter Finland.

CRediT authorship contribution statement

Jari Hyttinen: Conceptualization, Funding acquisition, Project administration, Resources, Supervision, Writing – original draft, Writing – review & editing. **Antti Paldanius:** Conceptualization, Data curation, Formal analysis, Investigation, Methodology, Resources, Software, Supervision, Validation, Visualization, Writing – original draft, Writing – review & editing. **Nina Fors:** Conceptualization, Validation, Writing – original draft, Writing – review & editing, Funding acquisition, Resources. **Jussi Toivanen:** Conceptualization, Data curation, Formal analysis, Investigation, Methodology, Resources, Software, Supervision, Validation, Visualization, Writing – original draft, Writing – review & editing. **Ville Kolehmainen:** Conceptualization, Funding acquisition, Project administration, Resources, Supervision, Writing – original draft, Writing – review & editing. **Daniel Strbian:** Conceptualization, Data curation, Funding acquisition, Resources, Validation, Writing – original draft, Writing – review & editing.

Declaration of Competing Interest

The authors declare that they have no competing financial interests or personal relationships that could influence the work reported in this paper.

Data availability

Data will be made available on request.

Acknowledgment

Model geometry data were provided in part by the Human Connectome Project, WU-Minn Consortium (Principal Investigators: David Van Essen and Kamil Ugurbil; 1U54MH091657) funded by the 16 NIH Institutes and Centers that support the NIH Blueprint for Neuroscience Research; and by the McDonnell Center for Systems Neuroscience at Washington University. The authors wish to acknowledge CSC - IT Center for Science, Finland, for computational resources. We thank Research Council of Finland, Jane and Aatos Erkkö Foundation and Neurocenter Finland for funding this research.

Appendix A. Supporting information

Supplementary data associated with this article can be found in the online version at [doi:10.1016/j.brainresbull.2025.111265](https://doi.org/10.1016/j.brainresbull.2025.111265).

References

- Angeli, S., Stylianopoulos, T., 2016. Biphasic modeling of brain tumor biomechanics and response to radiation treatment. *J. Biomech.* 49, 1524–1531. <https://doi.org/10.1016/j.jbiomech.2016.03.029>. (<https://www.sciencedirect.com/science/article/pii/S0021929016303335>).
- Arridge, S., Betcke, M., Harhanen, L., 2014. Iterated preconditioned LSQR method for inverse problems on unstructured grids. *Inverse Probl.* 30, 075009. <https://doi.org/10.1088/0266-5611/30/7/075009>.
- Atefi, S.R., Seoane, F., Kamalian, S., Rosenthal, E.S., Lev, M.H., Bonmassar, G., 2016. Intracranial hemorrhage alters scalp potential distribution in bioimpedance cerebral monitoring: preliminary results from fem simulation on a realistic head model and human subjects. *Med. Phys.* 43, 675–686.
- Avery, J., Aristovich, K., Low, B., Holder, D., 2017. Reproducible 3d printed head tanks for electrical impedance tomography with realistic shape and conductivity distribution. *Physiol. Meas.* 38, 1116–1131. <https://doi.org/10.1088/1361-6579/aa6586>.
- Bagshaw, A.P., Liston, A.D., Bayford, R.H., Tizzard, A., Gibson, A.P., Tidswell, A., Sparkes, M.K., Dehghani, H., Binnie, C.D., Holder, D.S., 2003. Electrical impedance tomography of human brain function using reconstruction algorithms based on the finite element method. *NeuroImage* 20, 752–764. [https://doi.org/10.1016/S1053-8119\(03\)00301-X](https://doi.org/10.1016/S1053-8119(03)00301-X). (<http://www.sciencedirect.com/science/article/pii/S105381190300301X>).
- Barber, D.C., Seagar, A.D., 1987. Fast reconstruction of resistance images. *Clin. Phys. Physiol. Meas.* 8, 47. <https://doi.org/10.1088/0143-0815/8/4A/006>.
- Bergström, J., 2015. 5 – elasticity/hyperelasticity. In: Bergström, J. (Ed.), *Mechanics of Solid Polymers*. William Andrew Publishing, pp. 209–307. <https://doi.org/10.1016/B978-0-323-31150-2.00005-4>. (<https://www.sciencedirect.com/science/article/pii/B9780323311502000054>).
- Bing, Y., Garcia-Gonzalez, D., Voets, N., Jérusalem, A., 2020. Medical imaging based in silico head model for ischaemic stroke simulation. *J. Mech. Behav. Biomed. Mater.* 101, 103442. <https://doi.org/10.1016/j.jmbmm.2019.103442>. (<https://www.sciencedirect.com/science/article/pii/S1751616119306162>).
- Broderick, J.P., Brott, T.G., Duldner, J.E., Tomsick, T., Huster, G., 1993. Volume of intracerebral hemorrhage. A powerful and easy-to-use predictor of 30-day mortality. *Stroke* 24, 987–993.
- Cheng, K., Isaacson, D., Newell, J., Gisser, D., 1989. Electrode models for electric current computed tomography. *IEEE Trans. Biomed. Eng.* 36, 918–924. <https://doi.org/10.1109/10.35300>.
- Culpepper, J., Lee, H., Santorelli, A., Porter, E., 2023. Applied machine learning for stroke differentiation by electrical impedance tomography with realistic numerical models. *Biomed. Phys. Eng. Express* 10, 015012. <https://doi.org/10.1088/2057-1976/ad0ad4>.
- Dai, M., Li, B., Hu, S., Xu, C., Yang, B., Li, J., Fu, F., Fei, Z., Dong, X., 2013. In vivo imaging of twist drill drainage for subdural hematoma: a clinical feasibility study on electrical impedance tomography for measuring intracranial bleeding in humans. *PLoS One* 8, e55020. <https://doi.org/10.1371/journal.pone.0055020>.
- Dai, M., Liu, X.C., Li, H.T., Xu, C.H., Yang, B., Wang, H., Shi, X.T., Dong, X.Z., Fu, F., et al., 2018. Eit imaging of intracranial hemorrhage in rabbit models is influenced by the intactness of cranium. *BioMed Res. Int.* 2018.
- Davis, S., Broderick, J., Hennerici, M., Brun, N., Diring, M., Mayer, S., Begtrup, K., Steiner, T., 2006. Hematoma growth is a determinant of mortality and poor outcome after intracerebral hemorrhage. *Neurology* 66, 1175–1181.
- Fouchar, A., Bonnet, S., Hervé, L., David, O., 2015. Flexible numerical platform for electrical impedance tomography. In: *Proceedings of the COMSOL Conference*. Grenoble.
- Gabriel, S., Lau, R., Gabriel, C., 1996. The dielectric properties of biological tissues: III. Parametric models for the dielectric spectrum of tissues. *Phys. Med. Biol.* 41, 2271. <https://doi.org/10.1088/0031-9155/41/11/003>.
- Goertz, L., Al-Sewaidi, Y., Habib, M., Zopfs, D., Reichardt, B., Ranft, A., Kabbasch, C., 2024. State-of-the-art mobile head ct scanner delivers nearly the same image quality as a conventional stationary ct scanner. *Sci. Rep.* 14, 6393.
- Goren, N., 2020. Clinical applications of electrical impedance tomography in stroke and traumatic brain injury.
- Goren, N., Avery, J., Dowrick, T., Mackle, E., Witkowska-Wrobel, A., Werring, D., Holder, D., 2018b. Multi-frequency electrical impedance tomography and neuroimaging data in stroke patients. *Sci. Data* 5, 1–10.
- Goren, N., Avery, J., Dowrick, T., Mackle, E., Witkowska-Wrobel, A., Werring, D., Holder, D., 2018a. Multi-frequency electrical impedance tomography and neuroimaging data in stroke patients. *Sci. Data* 5, 1–10. <https://doi.org/10.1038/sdata.2018.112>.
- Greenberg, S.M., Ziai, W.C., Cordonnier, C., Dowlatshahi, D., Francis, B., Goldstein, J.N., Hemphill III, J.C., Johnson, R., Keigher, K.M., Mack, W.J., et al., 2022. 2022 guideline for the management of patients with spontaneous intracerebral hemorrhage: a guideline from the American Heart Association/American Stroke Association. *Stroke* 53, e282–e361. <https://doi.org/10.1161/STR.0000000000000407>.
- Harhanen, L., Hyvönen, N., Majander, H., Staboulis, S., 2015. Edge-enhancing reconstruction algorithm for three-dimensional electrical impedance tomography. *SIAM J. Sci. Comput.* 37, B60–B78. <https://doi.org/10.1137/140971750>.
- He, Q., Rezaei, A., Pursiainen, S., 2020. Zeffiro user interface for electromagnetic brain imaging: a gpu accelerated fem tool for forward and inverse computations in matlab. *Neuroinformatics* 18, 237–250.
- Jehl, M., Aristovich, K., Faulkner, M., Holder, D., 2016. Are patient specific meshes required for EIT head imaging? *Physiol. Meas.* 37, 879.
- Kaipio, J., Kolehmainen, V., Somersalo, E., Vauhkonen, M., 2000. Statistical inversion and Monte Carlo sampling methods in electrical impedance tomography. *Inverse Probl.* 16, 1487–1522. <https://doi.org/10.1088/0266-5611/16/5/321>.
- Katan, M., Luft, A., 2018. Global burden of stroke. In: *Seminars in Neurology*. Thieme Medical Publishers, pp. 208–11. (<https://doi.org/10.1055/s-0038-1649503>).
- Kolehmainen, V., Ehrhardt, M.J., Arridge, S.R., 2019. Incorporating structural prior information and sparsity into EIT using parallel level sets. *Inverse Probl. Imaging* 13, 285–307. <https://doi.org/10.3934/ipi.2019015>.
- Lee, E., Duffy, W., Hadimani, R., Waris, M., Siddiqui, W., Islam, F., Rajamani, M., Nathan, R., Jiles, D., 2016. Investigational effect of brain-scalp distance on the efficacy of transcranial magnetic stimulation treatment in depression. *IEEE Trans. Magn.* 52, 1–4. <https://doi.org/10.1109/TMAG.2015.2514158>.
- Li, H., Chen, R., Xu, C., Liu, B., Tang, M., Yang, L., Dong, X., Fu, F., 2017. Unveiling the development of intracranial injury using dynamic brain eit: an evaluation of current reconstruction algorithms. *Physiol. Meas.* 38, 1776. <https://doi.org/10.1088/1361-6579/aa8016>.
- Lieberman, C., Willcox, K., Ghattas, O., 2010. Parameter and state model reduction for large-scale statistical inverse problems. *SIAM J. Sci. Comput.* 32, 2523–2542. <https://doi.org/10.1137/090775622>.
- Liu, D., Kolehmainen, V., Siltanen, S., Laukkanen, A.M., Seppänen, A., 2015. Estimation of conductivity changes in a region of interest with electrical impedance tomography. *Inverse Probl. Imaging* 9, 211–229. <https://doi.org/10.3934/ipi.2015.9.211>.
- Mayer, S.A., Frontera, J.A., Jankowitz, B., Kellner, C.P., Kuppermann, N., Naik, B.I., Nishijima, D.K., Steiner, T., Goldstein, J.N., Glynn, S., et al., 2021. Recommended primary outcomes for clinical trials evaluating hemostatic agents in patients with intracranial hemorrhage: a consensus statement. *JAMA Netw. Open* 4, e2123629.
- McDermott, B., McGinley, B., Krukiewicz, K., Divilly, B., Jones, M., Biggs, M., O'Halloran, M., Porter, E., 2017. Stable tissue-mimicking materials and an anatomically realistic, adjustable head phantom for electrical impedance tomography. *Biomed. Phys. Eng. Express* 4, 015003. <https://doi.org/10.1088/2057-1976/aa922d>.
- Mokri, B., 2001. The Monro–Kellie hypothesis: applications in csf volume depletion. *Neurology* 56, 1746–1748.
- Oostenveld, R., Praamstra, P., 2001. The five percent electrode system for high-resolution eeg and erp measurements. *Clin. Neurophysiol.* 112, 713–719.
- Ouyprongkochagorn, T., Polydorides, N., McCann, H., 2023. Towards continuous eit monitoring for hemorrhagic stroke patients. *Front. Physiol.* 14, 1157371.
- Paldanius, A., Dekdouk, B., Toivanen, J., Kolehmainen, V., Hyttinen, J., 2021. Sensitivity analysis highlights the importance of accurate head models for electrical impedance tomography monitoring of intracerebral hemorrhagic stroke. *IEEE Trans. Biomed. Eng.* 69, 1491–1501. <https://doi.org/10.1109/TBME.2021.3120929>.
- Pinho, J., Costa, A.S., Araújo, J.M., Amorim, J.M., Ferreira, C., 2019. Intracerebral hemorrhage outcome: a comprehensive update. *J. Neurol. Sci.* 398, 54–66.
- Poon, M.T.C., Fonville, A.F., Salman, R.A.S., 2014. Long-term prognosis after intracerebral haemorrhage: systematic review and meta-analysis. *J. Neurol. Neurosurg. Psychiatry* 85, 660–667.
- Renedo, D., Acosta, J.N., Leasure, A.C., Sharma, R., Krumholz, H.M., de Havenon, A., Alahdab, F., Aravkin, A.Y., Aryan, Z., Bärnighausen, T.W., Basu, S., Burkart, K., Coberly, K., Criqui, M.H., Dai, X., Desai, R., Dharmaratne, S.D., Doshi, R., Elgendy, I. Y., Feigin, V.L., Filip, I., Gad, M.M., Ghozy, S., Hafezi-Nejad, N., Kalani, R., Karaye, I.

- M., Kisa, A., Krishnamoorthy, V., Lo, W., Mestrovic, T., Miller, T.R., Misganaw, A., Mokdad, A.H., Murray, C.J.L., Natto, Z.S., Radfar, A., Ram, P., Roth, G.A., Seylani, A., Shah, N.S., Sharma, P., Sheikh, A., Singh, J.A., Song, S., Sotoudeh, H., Vervoort, D., Wang, C., Xiao, H., Xu, S., Zand, R., Falcone, G.J., Sheth, K.N., 2024. Burden of ischemic and hemorrhagic stroke across the US from 1990 to 2019. *JAMA Neurol.* (<https://doi.org/10.1001/jamaneurol.2024.0190>).
- Robinson, D., Van Sanford, C., Kwon, S.Y., Coleman, E., Sekar, P., Murphy, R., Flaherty, M.L., Demel, S.L., Aziz, Y., Moomaw, C.J., et al., 2022. What is the median volume of intracerebral hemorrhage and is it changing? *Int. J. Stroke* 17, 576–582. <https://doi.org/10.1177/17474930211032594>.
- Rudin, L., Osher, S., Fatemi, E., 1992. Nonlinear total variation based noise removal algorithms. *Phys. D: Nonlinear Phenom.* 60, 259–268. [https://doi.org/10.1016/0167-2789\(92\)90242-F](https://doi.org/10.1016/0167-2789(92)90242-F).
- Shi, Y., Wu, Y., Wang, M., Tian, Z., Kong, X., He, X., 2021. Sparse image reconstruction of intracerebral hemorrhage with electrical impedance tomography. *J. Med. Imaging* 8, 014501. <https://doi.org/10.1117/1.JMI.8.1.014501>.
- Somersalo, E., Cheney, M., Isaacson, D., 1992. Existence and uniqueness for electrode models for electric current computed tomography. *SIAM J. Appl. Math.* 52, 1023–1040. <https://doi.org/10.1137/0152060>.
- Toivanen, J., Hänninen, A., Savolainen, T., Forss, N., Kolehmainen, V., 2021. Monitoring hemorrhagic strokes using EIT. In: *Bioimpedance and Spectroscopy*. Elsevier, pp. 271–298. <https://doi.org/10.1016/B978-0-12-818614-5.00007-2>.
- Toivanen, J., Paldanius, A., Dekdouk, B., Candiani, V., Hänninen, A., Savolainen, T., Strbian, D., Forss, N., Hyvönen, N., Hyttinen, J., et al., 2024. Simulation-based feasibility study of monitoring of intracerebral hemorrhages and detection of secondary hemorrhages using electrical impedance tomography. *J. Med. Imaging* 11, 014502.
- Vauhkonen, M., Vadasz, D., Karjalainen, P.A., Somersalo, E., Kaipio, J.P., 1998. Tikhonov regularization and prior information in electrical impedance tomography. *IEEE Trans. Med. Imaging* 17, 285–293. <https://doi.org/10.1109/42.700740>.
- Vogel, C., 2002. Computational methods for inverse problems. Number 23 in *Frontiers in Applied Mathematics*. SIAM.
- Xiang, J., Dong, Y., Yang, Y., 2020. Multi-frequency electromagnetic tomography for acute stroke detection using frequency-constrained sparse bayesian learning. *IEEE Trans. Med. Imaging* 39, 4102–4112. <https://doi.org/10.1109/TMI.2020.3013100>.
- Xu, C.H., Wang, L., Shi, X.T., You, F.S., Fu, F., Liu, R.G., Dai, M., Zhao, Z.W., Gao, G.D., Dong, X.Z., 2010. Real-time imaging and detection of intracranial haemorrhage by electrical impedance tomography in a Piglet model. *J. Int. Med. Res.* 38, 1596–1604. <https://doi.org/10.1177/147323001003800504>.
- Yang, L., Liu, W., Chen, R., Zhang, G., Li, W., Fu, F., Dong, X., 2017. In vivo bioimpedance spectroscopy characterization of healthy, hemorrhagic and ischemic rabbit brain within 10 Hz to 1 mHz. *Sensors* 17, 791.
- Zhang, J., Yang, B., Li, H., Fu, F., Shi, X., Dong, X., Dai, M., 2017. A novel 3d-printed head phantom with anatomically realistic geometry and continuously varying skull resistivity distribution for electrical impedance tomography. *Sci. Rep.* 7, 4608.